PNAS
www.pnas.org

Supplementary Information for

Atomic-scale Evidence for Highly Selective Electrocatalytic N−N Coupling on Metallic MoS_2

Daoping He, Hideshi Ooka, Yujeong Kim, Yamei Li, Fangming Jin, Sun Hee Kim, Ryuhei Nakamura

Fangming Jin; Sun Hee Kim; Ryuhei Nakamura
Email: fmjin@sjtu.edu.cn; shkim7@kbsi.re.kr; ryuhei.nakamura@riken.jp

This PDF file includes:

www.pnas.org/cgi/doi/10.1073/pnas.2008429117

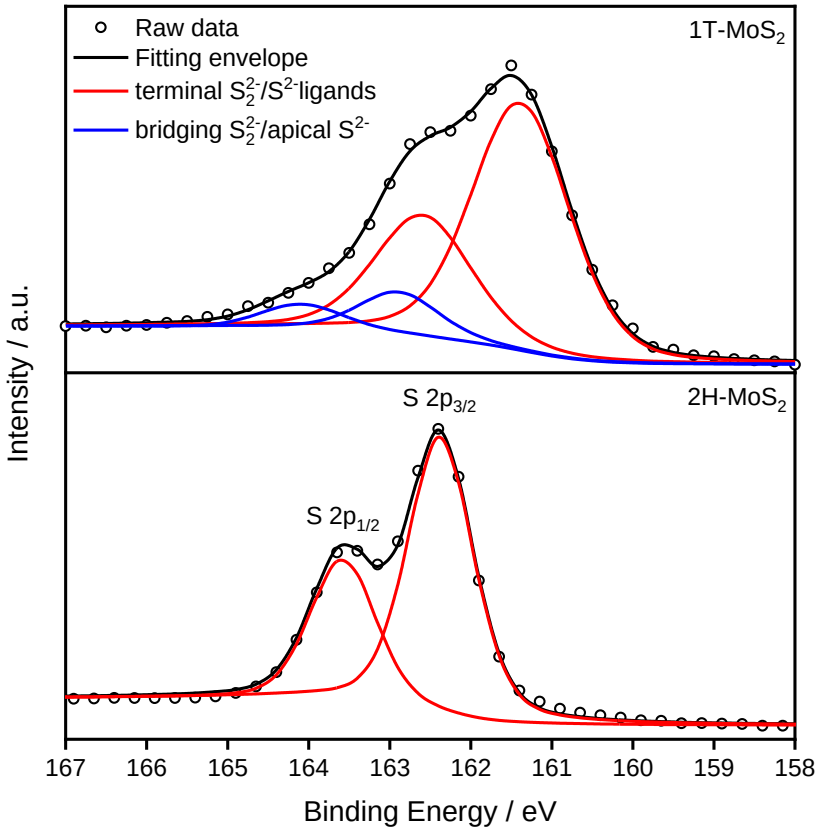

Fig. S1. XPS S 2*p* spectra of 1T-MoS_2 and 2H-MoS_2 and the deconvolution. The binding energies of the S 2*p* peaks are also shifted to smaller values for 1T-MoS_2. The sulfur peak was also separated into two doublets. The doublet with lower binding energy reflects the terminal S_2^{2-} and unsaturated S^{2-}, while the higher binding energy doublet is associated with apical S^{2-} and bridging S_2^{2-} (1-3). By integrating the intensities of characteristic S $2p_{1/2}$ and S $2p_{3/2}$ peaks, the percentage of apical S^{2-} and bridging S_2^{2-} with respect to terminal S_2^{2-} and unsaturated S^{2-} for 1T-MoS_2 was found to be 12.1%, confirming the existence of more sulfur-terminated edges in 1T-MoS_2. Detailed analysis of elemental compositions reveals that the atomic ratio of Mo:S is 1:1.9 for 1T-MoS_2 and 1:2.0 for 2H-MoS_2, respectively.

Table S1. Summary of the structural parameters of 1T-MoS_2 and 2H-MoS_2.

Sample	BE (Mo^{IV})[a)]	Higher BE (S)[b)]	Lower BE (S)[c)]	Atomic ratio of Mo/S	Ratio of 1T phase	P[d)]
2H-MoS_2	229.5 ($3d_{5/2}$), 232.7 ($3d_{3/2}$)	–	162.37 ($2p_{3/2}$), 163.57 ($2p_{1/2}$)	1:2.0	0%	0
1T-MoS_2	228.5 ($3d_{5/2}$), 231.7 ($3d_{3/2}$)	162.89 ($2p_{3/2}$), 164.09 ($2p_{1/2}$)	161.39 ($2p_{3/2}$), 162.59 ($2p_{1/2}$)	1:1.9	55%	12.1%

[a)] BE: Binding Energy (eV); [b)] Higher BE (S): bridging S_2^{2-} + apical S^{2-}; [c)] Lower BE (S): terminal S_2^{2-} + unsaturated S^{2-}; [d)] P: percentage of higher binding energy S.

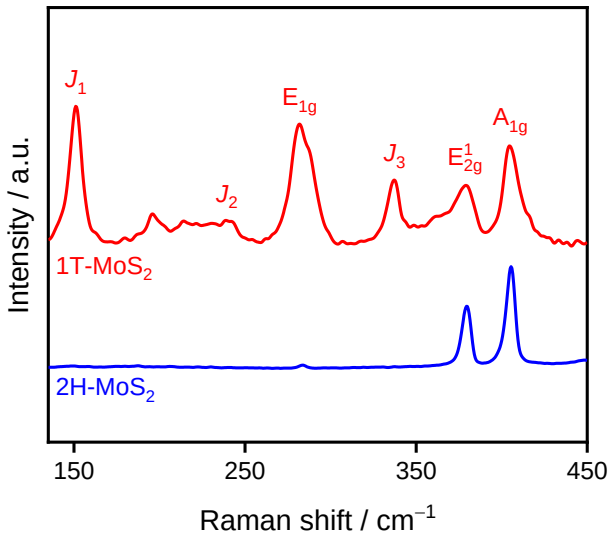

Fig. S2. Raman spectra of 1T-MoS_2 and 2H-MoS_2. The in-plane Mo−S phonon mode (E_{2g}) and out-of-plane S phonon mode (A_{1g}) are located at 379 and 405 cm^{-1}, respectively, confirming that 2H is the dominant phase for the commercial 2H-MoS_2 sample (4,5). In contrast, the 1T-MoS_2 sample shows additional peaks at 150 (J_1), 239 (J_2), and 337 cm^{-1} (J_3), respectively. The presence of these peaks is attributed to the superlattice structure in the Brillouin zone folding (6-8). Furthermore, the presence of the E_{1g} peak at 282 cm^{-1} confirms the dominant octahedral coordination of Mo in the 1T phase, together with the strong suppression of the E_{2g} and A_{1g} peaks (9). Experimental conditions: 532-nm laser; coadditions, 20 spectra; integration time, 10 s.

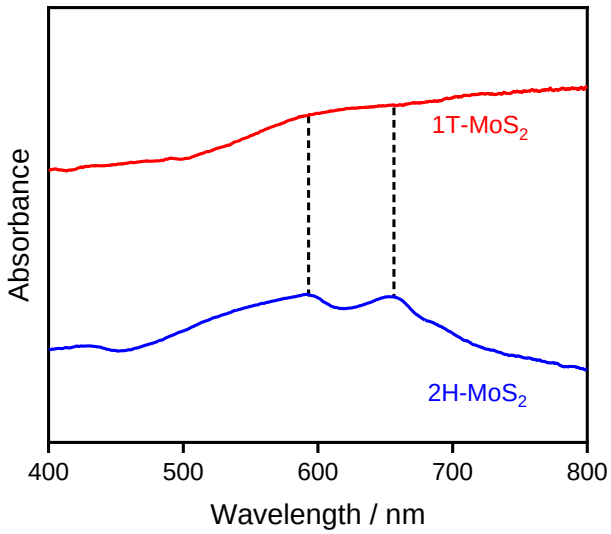

Fig. S3. UV-vis absorption spectra of 1T-MoS_2 and 2H-MoS_2. The UV-vis spectra of 1T-MoS_2 and 2H-MoS_2 powder were collected in diffuse transmission mode. Two typical absorption peaks located at 593 and 655 nm were observed for 2H-MoS_2. These peaks are assigned to the energy splitting from the valence band spin-orbital coupling, due to its semiconductive property (10). In contrast, the absorption spectrum of 1T-MoS_2 has no salient absorption bands but a monotonic change that is indicative of its metallic property (11).

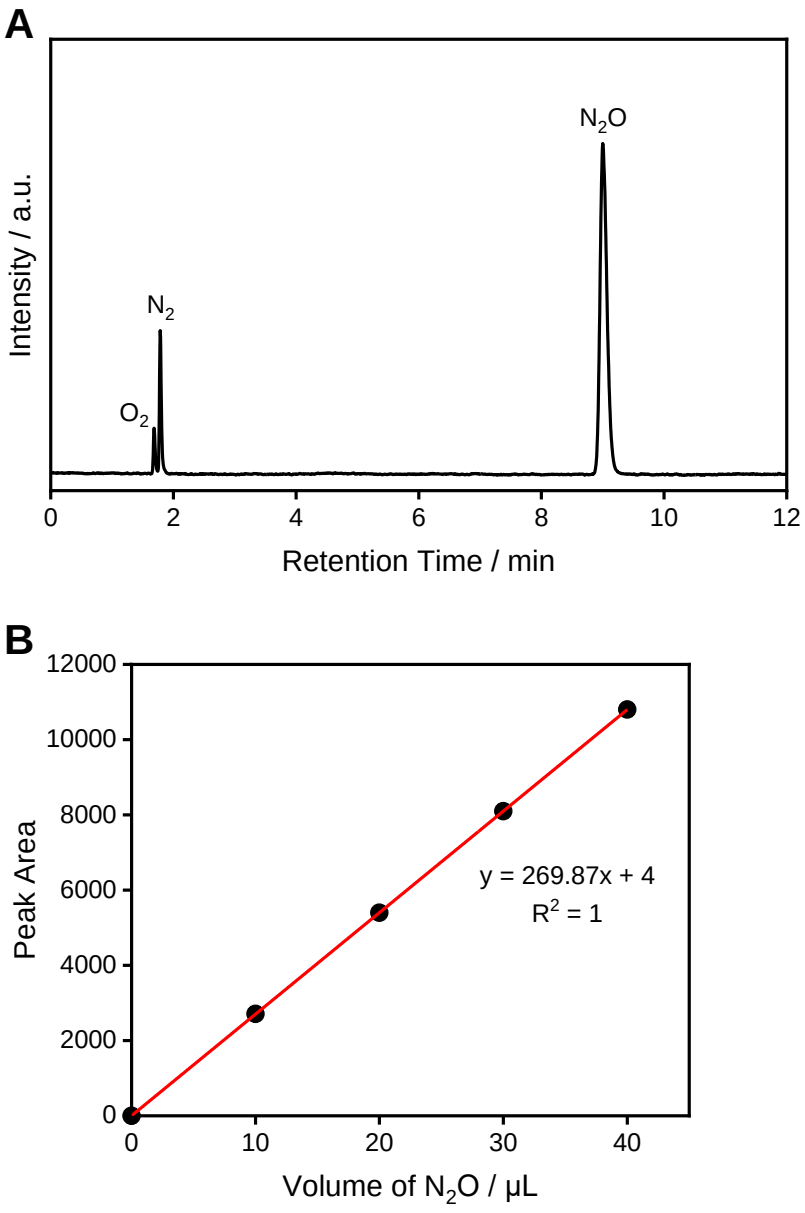

Fig. S4. GC calibration of N_2O. (A) Gas chromatography and (B) calibration curves of N_2O.

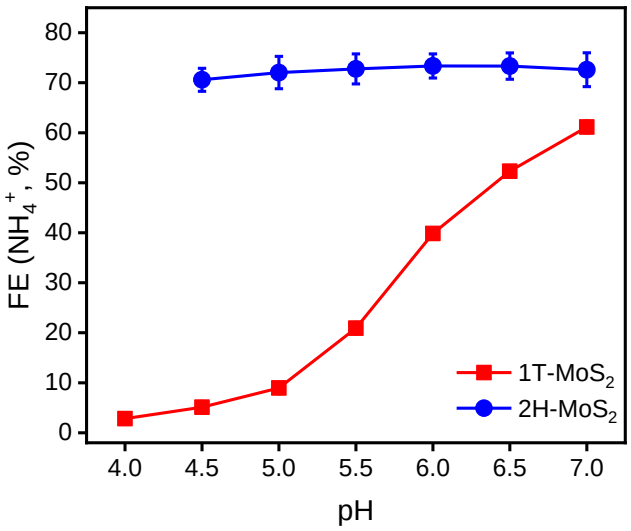

Fig. S5. Electroreduction of NO_2^- to NH_4^+ on MoS_2. Faradaic efficiency of NH_4^+ production via NO_2^- reduction (0.1 M) by 1T-MoS_2 and 2H-MoS_2 as a function of pH at 0.1 V vs RHE for 4 h.

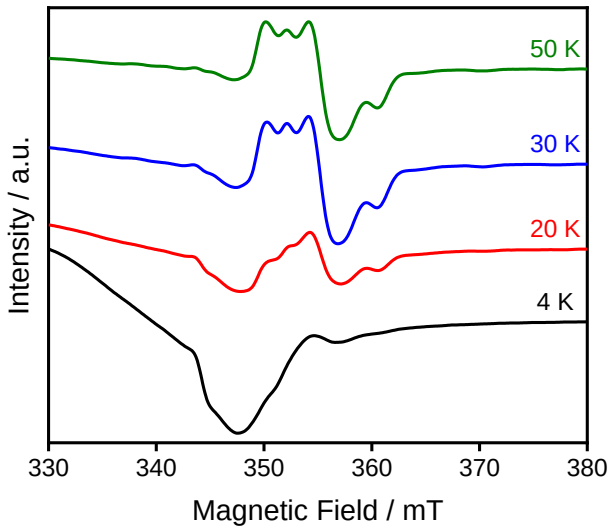

Fig. S6. Temperature-dependent EPR spectra of 1T-MoS_2. Temperature-dependent EPR spectra of 1T-MoS_2 in 20 mM dithionite solution at pH 5. Experimental conditions: microwave frequency, 9.64 GHz; microwave power, 1 mW; modulation frequency, 100 kHz; modulation amplitude, 1.0 mT; time constant, 40.96 ms; conversion time, 48.00 ms; sweep time, 96 s; four scans.

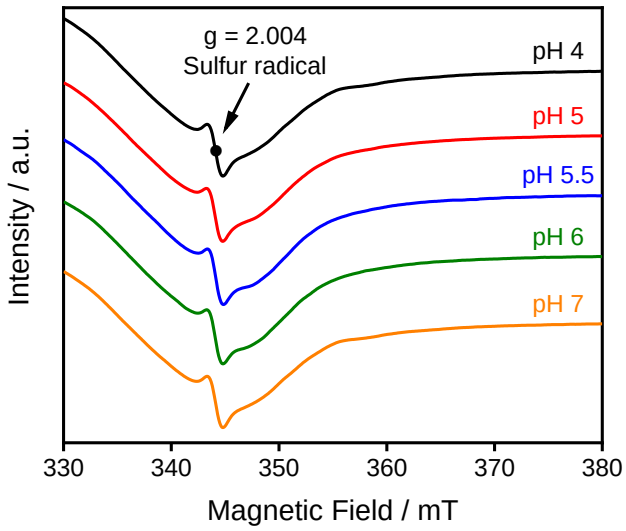

Fig. S7. EPR spectra of 1T-MoS_2 in the absence of dithionite. The EPR spectra of 1T-MoS_2 immersed in pure buffer solution. The buffer solution was prepared using either 0.2 M citric acid for pH 4, 5, and 5.5, or 0.2 M phosphate for pH 6 and 7, respectively. Experimental conditions: microwave frequency, 9.64 GHz; microwave power, 1 mW; modulation frequency, 100 kHz; modulation amplitude, 1.0 mT; time constant, 40.96 ms; conversion time, 48.00 ms; sweep time, 96 s; four scans.

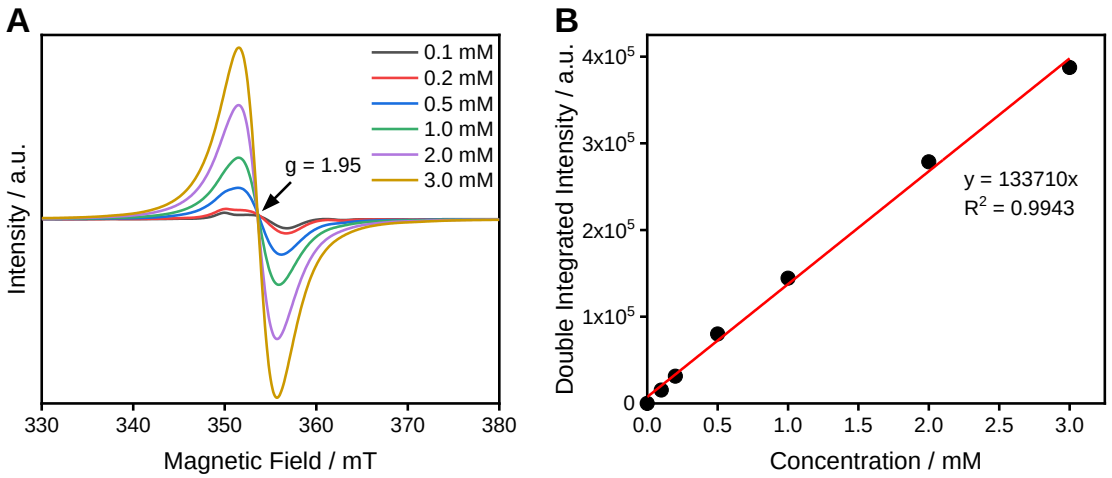

Fig. S8. EPR calibration of $MoCl_5$. (A) EPR spectra and (B) calibration curve of $MoCl_5$. The experiments were performed using $Mo^{V}Cl_5$ dissolved in acetonitrile. The calibration curve was obtained by double integrating the Mo^{V} EPR signal at different concentration of Mo^{V} and the concentration of the catalyst was determined by the interpolation of the calibration curve. Experimental conditions: microwave frequency, 9.64 GHz; microwave power, 1 mW; modulation frequency, 100 kHz; modulation amplitude, 1.0 mT; time constant, 40.96 ms; conversion time, 48.00 ms; sweep time, 96 s; four scans; temperature, 30 K.

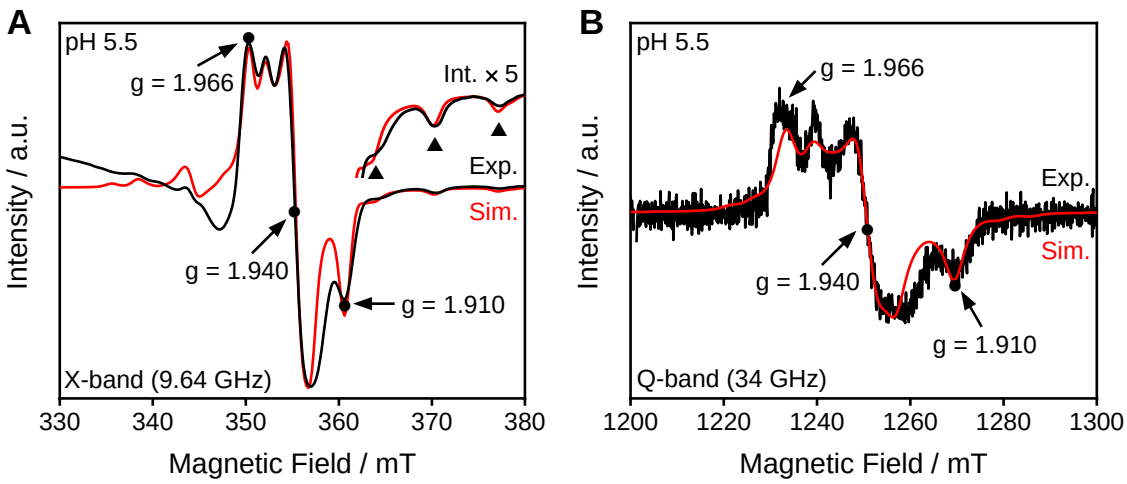

Fig. S9. EPR spectra of 1T-MoS_2 at pH 5.5. (A) X-band CW-EPR and (B) Q-band derivative ESE-detected EPR spectra of 1T-MoS_2 generated after reduction by 20 mM dithionite at pH 5.5. (black: experimental spectra, red: simulated spectra). To obtain detailed structural information of the pH-dependent Mo^V species, X-band (9.6 GHz) and Q-band (34 GHz) CW-EPR experiments were carried out. At pH 5.5, the X-band and the Q-band EPR data display a rhombic signal with g = [1.966, 1.940, 1.910], suggesting that the local geometry of the Mo^V is significantly anisotropic. Clear low-intensity satellite peaks (indicated as solid triangles in the inset of A) were observed due to hyperfine coupling of ^{95}Mo (I = 5/2) (12-15). We determine the hyperfine coupling constants of the ^{95}Mo to be A (^{95}Mo) = [130, < 50, 175] by simulating these satellite peaks. The spectrum is less sensitive to the A_2 (^{95}Mo) value, and does not change significantly until the A_2 (^{95}Mo) is increased to more than 50 MHz. Experimental conditions: microwave frequency, 9.64 GHz; microwave power, 1 mW; modulation frequency, 100 kHz; modulation amplitude, 1.0 mT; time constant, 40.96 ms; conversion time, 48.00 ms; sweep time, 96 s; four scans.

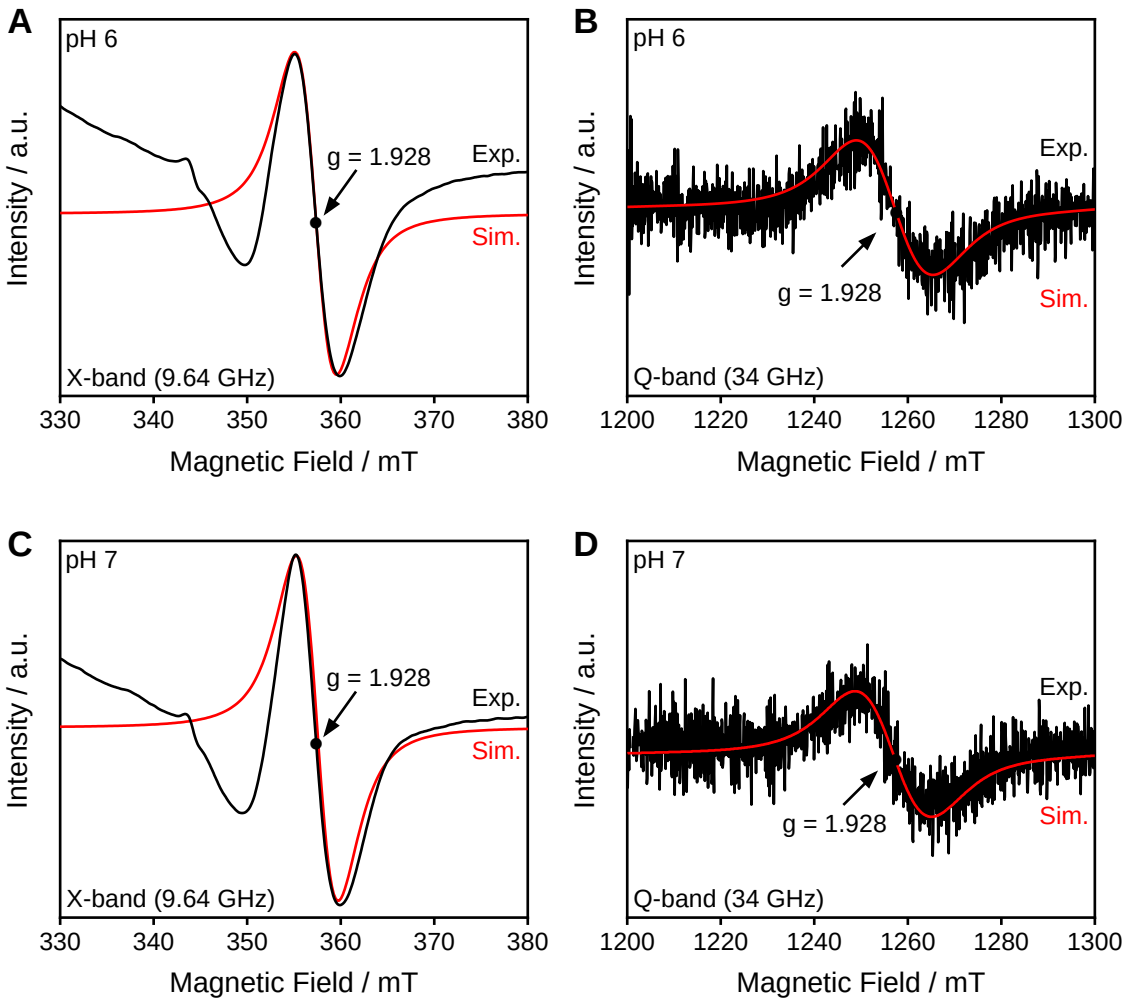

Fig. S10. EPR spectra of 1T-MoS_2 at pH 6 and 7. X-band CW-EPR and Q-band derivative ESE-detected EPR spectra of 1T-MoS_2 generated after reduction by 20 mM dithionite at pH 6 (A, B) and 7 (C, D). (black: experimental spectra, red: simulated spectra). The X-band and the Q-band EPR spectrum of Mo^V species only exhibit an isotropic signal (g = 1.928). Experimental conditions: microwave frequency, 9.64 GHz; microwave power, 1 mW; modulation frequency, 100 kHz; modulation amplitude, 1.0 mT; time constant, 40.96 ms; conversion time, 48.00 ms; sweep time, 96 s; four scans.

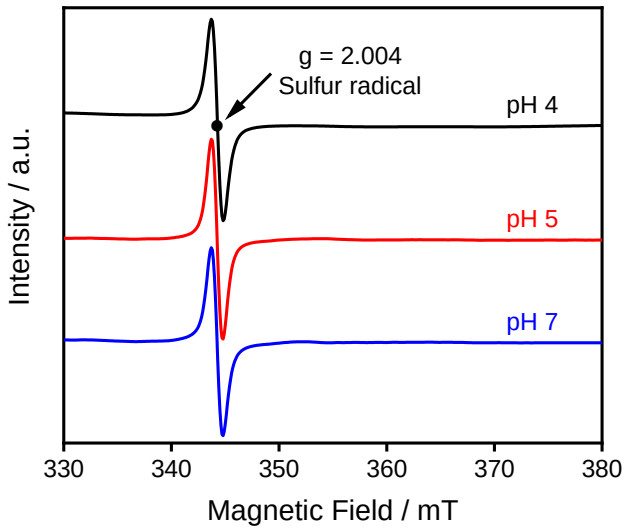

Fig. S11. EPR spectra of 2H-MoS_2. The EPR spectra of 2H-MoS_2 immersed in 20 mM dithionite solution. No changes in the EPR spectrum (350 ~ 370 mT) were observed by changing the pH. Experimental conditions: microwave frequency, 9.64 GHz; microwave power, 1 mW; modulation frequency, 100 kHz; modulation amplitude, 1.0 mT; time constant, 40.96 ms; conversion time, 48.00 ms; sweep time, 96 s; four scans.

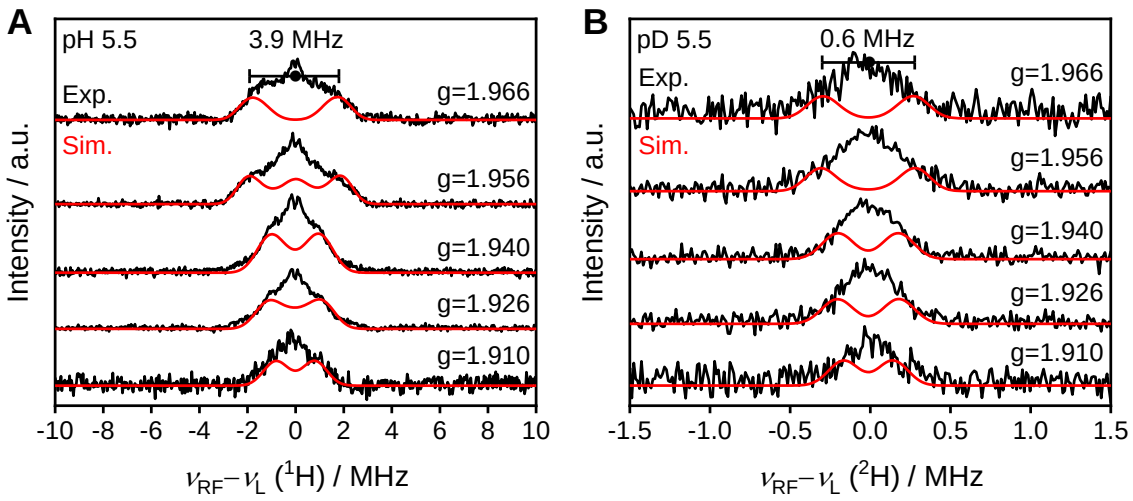

Fig. S12. ENDOR spectra of 1T-MoS_2 at pH 5.5. (A) The 2D field-dependent ^{1}H Davies ENDOR and (B) ^{2}H Mims ENDOR spectra of 1T-MoS_2 generated after reduction by 20 mM dithionite at pH 5.5 (black lines). The simulated spectra are shown in red. The simulations parameters are as follows: panel A: A = [−3.4, 4.5, 2.5] MHz, Euler Angle = [α, β, γ] = [90, 115, 20]°; panel B: A = [−0.5, 0.7, 0.4] MHz, Euler Angle = [α, β, γ] = [90, 115, 20]°. Experimental conditions: microwave frequency, 34 GHz; T = 30 K; Davies ENDOR π/2 width, 32 ns, τ = 400 ns, RF pulse width, 20 μs; Mims ENDOR π/2 width, 32 ns, τ = 200 ns, RF pulse width, 40 μs.

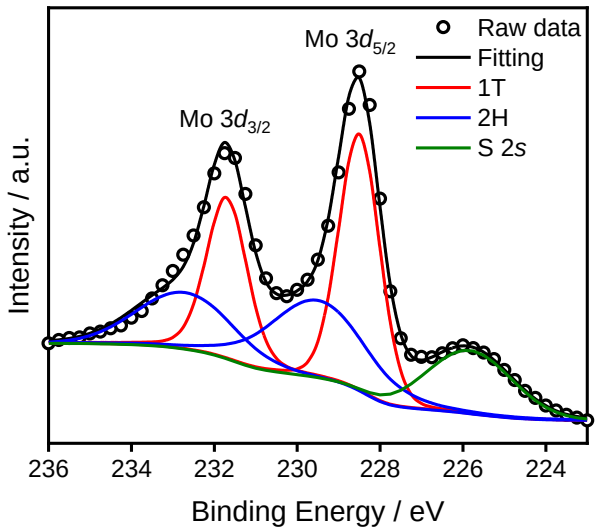

Fig. S13. Stability of 1T-MoS_2. The Mo 3*d* XPS spectra of 1T-MoS_2 along with the spectral deconvolution after NO_2^- reduction (0.1 M) at pH 5 for 4 h at 0.1 V vs RHE.

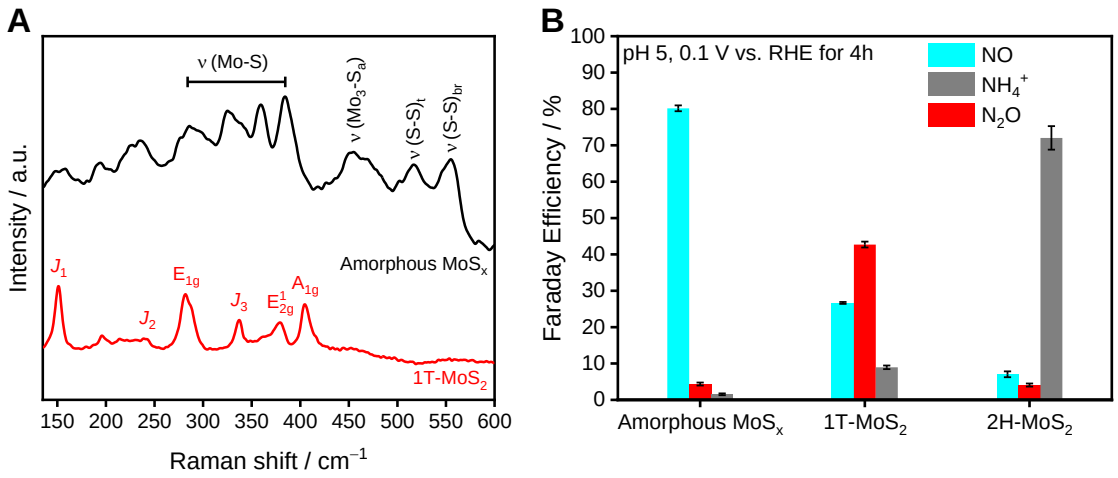

Fig. S14. Raman spectra and electrocatalytic performance of amorphous MoS_x. (A) Raman spectra of amorphous MoS_x. (B) The electrocatalytic performance of amorphous MoS_x toward NO_2^- reduction at pH 5 and 0.1 V vs RHE for 4 h. The amorphous MoS_x was synthesized by electrochemical deposition at room temperature (15). As shown in (A), the spectrum of hydrothermally synthesized 1T-MoS_2 showed clear Raman bands assigned to the 1T phase, and no bands assignable to the amorphous MoS_x was resolved under the detection limit of Raman spectroscopy. Furthermore, the electrocatalytic performance in (B) demonstrated that amorphous MoS_x selectively produces NO (FE: ~ 80%) and has negligible activity towards N_2O production (FE: ~ 4%), thus ruling out amorphous MoS_x as the possible catalytic site for selective N−N coupling.

SI References

1. Huang, L.B. *et al.* Self-Limited on-Site Conversion of MoO_3 Nanodots into Vertically Aligned Ultrasmall Monolayer MoS_2 for Efficient Hydrogen Evolution. *Adv. Energy Mater.* **8**, 1800734 (2018).
2. Ting, L.R.L. *et al.* Catalytic Activities of Sulfur Atoms in Amorphous Molybdenum Sulfide for the Electrochemical Hydrogen Evolution Reaction. *ACS Catal.* **6**, 861-867 (2016).
3. Deng, Y.L. *et al.* Operando Raman Spectroscopy of Amorphous Molybdenum Sulfide (MoS_x) during the Electrochemical Hydrogen Evolution Reaction: Identification of Sulfur Atoms as Catalytically Active Sites for H^+ Reduction. *ACS Catal.* **6**, 7790-7798 (2016).
4. Ding, W. *et al.* Highly Ambient-Stable 1T-MoS_2 and 1T-WS_2 by Hydrothermal Synthesis under High Magnetic Fields. *ACS Nano* **13**, 1694-1702 (2019).
5. Yu, Y. *et al.* High phase-purity 1T'-MoS_2- and 1T'-$MoSe_2$-layered crystals. *Nat. Chem.* **10**, 638-643 (2018).
6. Liu, Q. *et al.* Gram-Scale Aqueous Synthesis of Stable Few-Layered 1T-MoS_2: Applications for Visible-Light-Driven Photocatalytic Hydrogen Evolution. *Small* **11**, 5556-5564 (2015).
7. Calandra, M. Chemically exfoliated single-layer MoS_2: Stability, lattice dynamics, and catalytic adsorption from first principles. *Phys. Rev. B* **88**, 245428 (2013).
8. Jiménez Sandoval, S., Yang, D., Frindt, R.F. & Irwin, J.C. Raman study and lattice dynamics of single molecular layers of MoS_2. *Phys. Rev. B* **44**, 3955-3962 (1991).
9. Cheng, P., Sun, K. & Hu, Y.H. Memristive Behavior and Ideal Memristor of 1T Phase MoS_2 Nanosheets. *Nano Lett.* **16**, 572-576 (2016).
10. Purcell-Milton, F. *et al.* Induction of Chirality in Two-Dimensional Nanomaterials: Chiral 2D MoS_2 Nanostructures. *ACS Nano* **12**, 954-964 (2018).
11. Geng, X. *et al.* Pure and stable metallic phase molybdenum disulfide nanosheets for hydrogen evolution reaction. *Nat. Commun.* **7**, 10672 (2016).
12. Busetto, L., Vaccari, A. & Martini, G. Electron-Spin Resonance of Paramagnetic Species as a Tool for Studying the Thermal-Decomposition of Molybdenum Trisulfide. *J. Phys. Chem.* **85**, 1927-1930 (1981).
13. Konings, A.J.A. *et al.* ESR studies on hydrodesulfurization catalysts: Supported and unsupported sulfided molybdenum and tungsten catalysts. *J. Catal.* **54**, 1-12 (1978).
14. Basu, P. Use of EPR Spectroscopy in Elucidating Electronic Structures of Paramagnetic Transition Metal Complexes. *J. Chem. Educ.* **78**, 666-669 (2001).
15. Tran, P.D. *et al.* Coordination polymer structure and revisited hydrogen evolution catalytic mechanism for amorphous molybdenum sulfide. *Nat. Mater.* **15**, 640-646 (2016).